Atom Probe Tomography Analysis of Ag Doping in 2D Layered Material $(PbSe)_5(Bi_2Se_3)_3$

Xiaochen Ren,[†] Arunima K. Singh,[‡] Lei Fang,[§,‖] Mercouri G. Kanatzidis,[§,‖] Francesca Tavazza,[‡] Albert V. Davydov,[‡] and Lincoln J. Lauhon*,[†]

[†]Department of Materials Science and Engineering, Northwestern University, 2220 Campus Drive, Evanston, Illinois 60208, United States

[‡]Materials Science and Engineering Division, National Institute of Standards and Technology, 100 Bureau Drive, Gaithersburg, Maryland 20899, United States
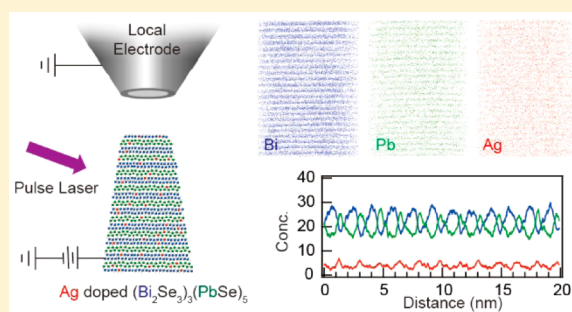
[§]Department of Chemistry, Northwestern University, 2145 Sheridan Road, Evanston, Illinois 60208, United States

[‖]Materials Science Division, Argonne National Laboratory, 9700 South Cass Avenue, Argonne, Illinois 60439, United States

Ⓢ *Supporting Information*

ABSTRACT: Impurity doping in two-dimensional (2D) materials can provide a route to tuning electronic properties, so it is important to be able to determine the distribution of dopant atoms within and between layers. Here we report the tomographic mapping of dopants in layered 2D materials with atomic sensitivity and subnanometer spatial resolution using atom probe tomography (APT). APT analysis shows that Ag dopes both Bi_2Se_3 and PbSe layers in $(PbSe)_5(Bi_2Se_3)_3$, and correlations in the position of Ag atoms suggest a pairing across neighboring Bi_2Se_3 and PbSe layers. Density functional theory (DFT) calculations confirm the favorability of substitutional doping for both Pb and Bi and provide insights into the observed spatial correlations in dopant locations.

KEYWORDS: *Atom probe tomography, doping, 2D materials, DFT, materials genome initiative*

Two-dimensional (2D) materials have attracted significant attention due to their unique physical properties[1−5] and potential in device applications.[6−10] Impurity doping plays a central role in controlling the properties of electronic materials and is beginning to be explored in 2D materials to modulate carrier density,[11,12] engineer the bandgap,[13] and impart magnetic properties.[14,15] One key challenge in doping 2D materials is to measure the dopant distribution, ideally with atomic resolution. Transmission electron microscopy (TEM) and scanning transmission electron microscopy (STEM) have been used to assess the in plane dopant distribution in 2D materials,[12,13,15−17] but atomic resolution in the vertical direction is not routinely achieved. Secondary ion mass spectrometry (SIMS) can reach atomic-scale resolution in depth profiling 2D materials, but its lateral resolution is on the order of 100 nm.[18] Here we report the use of atom probe tomography (APT) and first-principles calculations to characterize the atomic scale distribution of Ag dopant atoms in $(PbSe)_5(Bi_2Se_3)_3$, a topological insulator material that can be rendered superconducting by doping with Ag. APT has been used to characterize the three-dimensional dopant distribution in nanowires,[19,20] thin films,[21] and FinFET devices,[22,23] but it has not previously been applied to analyze doping in 2D materials. Here, we define 2D materials as materials in which interactions between layers are primarily van der Waals in

nature, enabling exfoliation by appropriate techniques. By this definition, $(PbSe)_5(Bi_2Se_3)_3$ can be considered as a 2D material (Supporting Information Figure S2).

A significant fraction of the research on 2D materials beyond graphene has focused on transition metal dichalcogenides (TMDs) that can be readily exfoliated and fabricated into conventional electronic devices such as transistors and photodetectors. However, many other layered materials beyond TMDs have intriguing electronic properties that are dramatically impacted by doping. For example, Bi_2Se_3 is a topological insulator,[5] whereas Cu-doped Bi_2Se_3 is a superconductor.[24] Superconductivity in $Cu_xBi_2Se_3$ is believed to arise from intercalated Cu,[24] but the ratio of intercalated and substitutional Cu atoms is unknown due to experimental limitations in characterizing the atomic scale dopant distribution. $(PbSe)_5(Bi_2Se_3)_{3m}$ is another promising system of homologous materials that consists of m layers of Bi_2Se_3 alternating with a layer of PbSe.[25] With an interlayer interaction of van der Waals type, this material can be easily exfoliated into 2D flakes. The $m = 2$ phase is a topological insulator[26] that can be made superconducting by Cu doping,[27,28] whereas the semimetallic m

= 1 phase can be made superconducting by Ag doping.[29] In this material system, one could in principle create an interface between a superconductor and topological insulator, which has been proposed to host Majorana Fermions.[30] Determination of the dopant location is an important step in improving understanding of the material synthesis and properties that could enable fundamentally new types of electronic properties and devices.

Toward this end, APT was used to analyze the location of Ag dopants in Ag-doped $(PbSe)_5(Bi_2Se_3)_3$. Despite previous assumptions that Ag atoms would substitute for Pb,[29] Ag is found to dope both Bi_2Se_3 and PbSe layers by APT, and radial distribution functions suggest attractive interactions between Ag atoms. Density functional theory (DFT) calculations of configuration formation energies show that the lowest energy doping configurations involve Ag atoms in each layer. The structural and charge analysis of Ag-doped $(PbSe)_5(Bi_2Se_3)_3$ simulated system reveals that the Ag atoms distort the lattice of $(PbSe)_5(Bi_2Se_3)_3$ due to lower electropositivity of Ag atoms in comparison to Pb and Bi atoms. The distortion of the lattice is expected to be energetically unfavorable as it is experimentally determined that more than 25% substitution of Ag in the $(PbSe)_5(Bi_2Se_3)_3$ renders the material unstable.[28] The precise determination of the Ag distribution may inform understanding of the origin of superconductivity in $(PbSe)_5(Bi_2Se_3)_3$ and provide insights as to how to approach the challenge of controlled doping in 2D materials. This work also demonstrates the potential for APT to characterize doping in 2D materials.

The Ag-doped $(PbSe)_5(Bi_2Se_3)_3$ was grown by solid state synthesis[29] with a nominal composition of $x \approx 1$ in $Ag_xPb_5Bi_6Se_{14}$, corresponding to a nominal Ag atomic concentration of 0.038. The crystal structure in Figure 1a shows alternately stacked Bi_2Se_3 and PbSe layers, and the weak interlayer bonding is revealed by the fracture surface observed in scanning electron microscopy imaging (Figure 1b). Specimens for APT analysis were prepared using standard focused ion beam (FIB) lift-out and sharpening procedures,[31] with the analysis direction perpendicular to (001) planes. The final

specimens were sharp needle-shaped tips with diameters less than 100 nm (Figure 1c). APT analysis was performed using a LEAP 4000X Si system* (*reference to commercial equipment does not imply NIST recommendation or endorsement) with 355 nm laser of 30 pJ pulse energy and 250 kHz pulse frequency, a 0.005 ions/pulse target detection rate, and a specimen temperature of 28 K. Of the pulse energies tried, 30 pJ gave the best spatial resolution (see Supporting Information Section 3). Figure 1d shows a three-dimensional reconstruction of a portion of the specimen (the overall reconstruction is given in Figure S1a), mapping Bi atoms as blue dots and Pb atoms as green dots. Alternating layered regions enriched in Bi and Pb layers are visible in the entire reconstruction and occur with the expected periodicity based on the crystal structure (Figure 1a).

A major motivation for APT doping analysis is the ability to detect single ions with very high spatial resolution. The laser conditions were chosen to optimize the spatial resolution in the analysis direction (Supporting Information Figure S3). The mass spectrum with the chosen laser conditions is shown in Figure 2a. No impurity peaks were detected, and the signal-to-
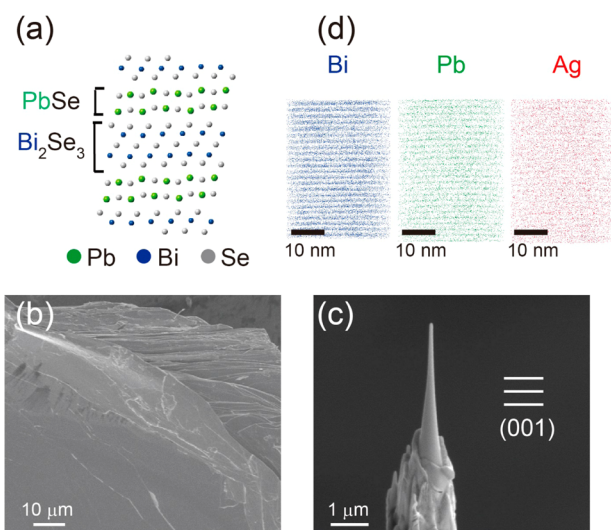
Figure 1. (a) Crystal structure of $(PbSe)_5(Bi_2Se_3)_3$ with alternating PbSe and Bi_2Se_3 layers. (b) Top view SEM image of the $(PbSe)_5(Bi_2Se_3)_3$ crystal. (c) SEM image of a sharpened tip. (d) A region of interest in the reconstruction with the distribution of Bi, Pb ,and Ag, showing that layers are resolved.
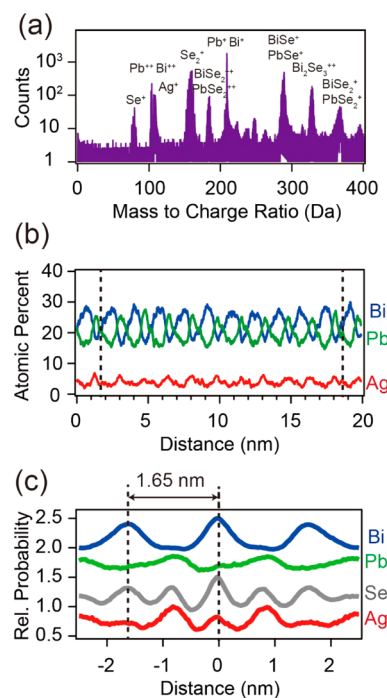
Figure 2. (a) Mass spectrum taken at 30 pJ laser pulse energy. (b) One-dimensional concentration profiles in the region of interest shown in Figure 1d. Dashed black lines indicate a distance of 10 lattice constants. (c) SDM of atoms relative to Bi atoms (curves are offset by 0.5 units each for clarity).

noise level establishes an upper bound of 100 ppm. Peaks for Bi^+/Pb^+ and Bi^{++}/Pb^{++} ions can be separated despite the small mass difference between Bi (209 Da) and Pb (204 Da, 206 Da, 207 Da, 208 Da). Peaks for complex ions, such as $BiSe^+$ and $PbSe^+$, $BiSe_2^{+2}$, and $PbSe_2^{+2}$, overlap due to the large spread of Se isotopes (74 to 82 Da). The overlap in peaks in the mass spectrum mixes the assignments of a small fraction of the complex ions, leading to some artificial *spatial* overlap of Bi and Pb elements (Figure 2b). (Ag is only detected as Ag^+ ions, which do not overlap with other ions in mass spectrum. Therefore, the 1D concentration profile of Ag does not suffer from spatial overlapping as discussed later.) Despite the

overlap, alternating Bi_2Se_3 and PbSe layers are resolved in Figure 2b. For a more quantitative statistical analysis of the spatial resolution, we performed a spatial distribution map (SDM) analysis by only counting nonoverlapped Bi^+/Pb^+ and Bi^{++}/Pb^{++} ions for Bi/Pb. Figure 2c presents the SDM of atoms in the vertical direction of the reconstruction using Bi atoms as the reference species. Briefly, a SDM reports the distribution of one species relative to other atoms of the same or different species. The peak distance in the Bi−Bi profile shows the lattice spacing to be 1.65 nm in the analysis direction, in agreement with the crystal structure. Furthermore, the peaks at ±0.85 nm in the Bi−Pb profile indicate that Bi atoms and Pb atoms are separated statistically from each other, i.e., Bi_2Se_3 and PbSe layers are resolved. In support of this interpretation, a similar analysis of $(PbSe)_5(Bi_2Se_3)_6$ is provided in the Supporting Information (Figure S4).

However, atomic planes within the Bi_2Se_3 and PbSe layers are not resolved. The imaging of atomic planes requires a well-defined field evaporation sequence in which atoms from the edges of terraces are first to leave the surface.[32,33] Atomic planes are often observed in metals, but less often in semiconductors due to penetration of electric field.[33] Although $(PbSe)_5(Bi_2Se_3)_3$ is semimetallic, the weak van der Waals interactions between layers may result in the simultaneous evaporation of many atoms in the same layer, which will hinder the imaging of atomic planes *within* the layers. This assumption is consistent with the experimental observation that the fraction of multiple hits varies nonmonotonically between 66% and 71% in steady evaporation. To our knowledge, APT has not been used previously to analyze 2D materials, with the exception of one recent report of impurity analysis in a graphene monolayer,[34] where the imaging of atomic planes was not achieved. So it remains an open question whether atomic planes can be resolved in APT of 2D materials.

The 1D concentration profile of Ag in Figure 2b shows two peaks in a lattice period, with large peaks in the same positions as the Pb peaks and small peaks in the same positions as the Bi peaks, indicating that Ag atoms are located in both PbSe and Bi_2Se_3 layers. SDM analysis of the Bi-centered Ag distribution (Bi−Ag profile, Figure 2c) shows more clearly that there are peaks at 0 nm and ±0.825 nm. The peaks at ±0.825 nm confirm that Ag atoms reside in the PbSe layers, while peak at 0 nm implies that Ag atoms also reside in the Bi_2Se_3 layers. To determine the local concentration of Ag in Bi_2Se_3 and PbSe layers, the one-dimensional composition profile between the two lines in Figure 2b was broken up into 10 segments, with the length of each segment equal to the lattice constant. The 10 segments were averaged together to determine the local Ag concentration (Figure 3a). The atomic concentration of Ag is 3.5% in the Bi_2Se_3 layer and peaks at 4.5% in the PbSe layer. Approximately 54% (46%) of the Ag atoms are detected in the Bi_2Se_3 (PbSe) layers. This direct measurement of local concentration is one of the most important capabilities of APT.

To provide further insights into the Ag distribution, first-principles DFT calculations were used to search for energetically favorable configurations of Ag atoms. A substitution of Ag atoms on Pb and Bi sites is expected due to the similarity in the covalent radii and valences. The nominal concentration of 0.038 can be simulated by substituting two Ag atoms in the 50 atom ($a = 16.3312$ Å, $b = 4.2635$ Å, and $c = 21.9245$ Å) monoclinic primitive cell of $(PbSe)_5(Bi_2Se_3)_3$ resulting in a 0.040 nominal concentration of Ag. The formation energies, ΔE_{Ag}^i, of all configurations with the two Ag atoms restricted to
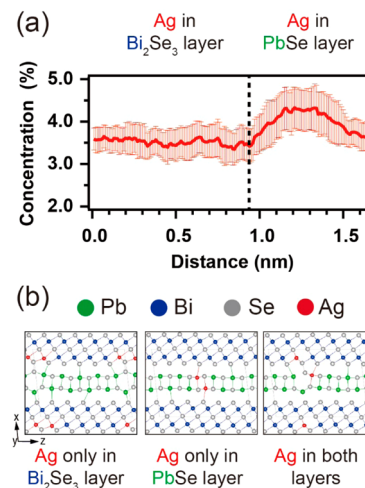

Figure 3. (a) One-dimensional concentration profile of Ag obtained by averaging the data shown in Figure 2b over 10 lattice constants. Error bars give the standard deviation. (b) Schematics of example configurations of Ag dopant atoms with Ag restricted to Pb sites, Bi sites, and equally distributed between Pb and Bi sites, respectively. The *y* direction is normal to the plane of the figure.

Pb-sites in the PbSe layer (45 configurations), Ag atoms restricted to Bi-sites in the Bi_2Se_3 layer (66 configurations), and Ag atoms distributed equally between Pb-sites and Bi-sites (120 configurations) are computed. A schematic of a configuration with Ag restricted to Pb-sites, Bi-sites and equally distributed in the Pb- and Bi-sites is shown in Figure 3b. ΔE_{Ag}^i of the *i*th configuration is given by

$$\Delta E_{Ag}^i = E_{Ag}^i - E - n_{Ag}\mu_{Ag} + n_{Pb}\mu_{Pb} + n_{Bi}\mu_{Bi}$$

where ΔE_{Ag}^i is the energy of the Ag substituted $(PbSe)_5(Bi_2Se_3)_3$ crystal in the *i*th configuration and E is the energy of the perfect $(PbSe)_5(Bi_2Se_3)_3$ crystal. The number of Ag atoms in the crystal is denoted by n_{Ag} and the number of these Ag atoms on the Pb- and Bi-sites is denoted by n_{Pb} and n_{Bi}, respectively. The phase diagram of PbSe−Bi_2Se_3 system indicates that all the constituent phases are in molten state at the 1223 K synthesis temperature of the crystal;[35] hence, the chemical potential of Ag, Pb, and Bi atoms, μ_{Ag}, μ_{Pb}, and μ_{Bi}, respectively, are taken to be the energies of the isolated atoms.

Figure 4a shows the formation energies of the configurations plotted against the distance between the Ag atoms. The distance between the Ag atoms is computed by ignoring the self-images in the periodic images. The formation energies of configurations with Ag atoms equally distributed on the Pb- and Bi-sites are significantly lower than those with Ag atoms restricted to the Pb-sites or Bi-sites only. Figure 4b shows the thermodynamic probability of occurrence of the *i*th configuration computed as

$$P^i = \frac{e^{(-\Delta E_{Ag}^i/k_B T)}}{\sum_{i=1-231} e^{(-\Delta E_{Ag}^i/k_B T)}}$$

where k_B is the Boltzmann constant and temperature $T = 300$ K. At room temperature, configurations with Ag in both layers account for more than 99.99% of the total probabilities. Even at temperatures as high as 923 K, configurations with Ag in both layers account for more than 97.57% of the total probabilities. Thus, the DFT calculations support the experimental
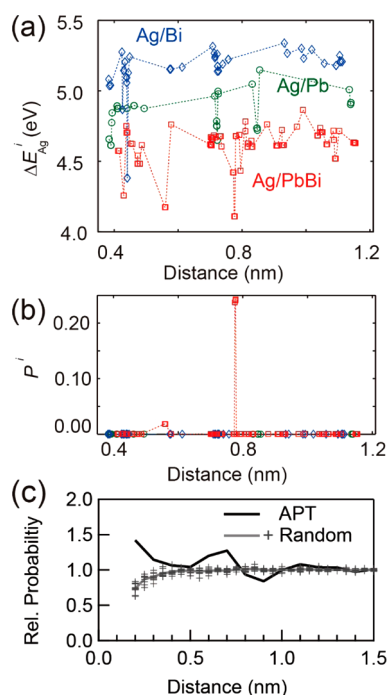
Figure 4. (a) Defect formation energies of different configurations of Ag dopants plotted against distance between pairs of Ag atoms. (b) Probabilities of occurrence of Ag–Ag configurations at 300 K. (c) Ag–Ag radial distribution function from APT reconstruction compared with that of Ag atoms randomly substituted for Bi and Pb atoms. Crosses show data points from individual distribution functions, and the gray line shows the average of 10 simulated distribution functions.

observation that Ag dopants are distributed between both Pb and Bi layers.

For the analysis above, all 231 possible configurations were simulated for the *primitive* cell of $(PbSe)_5(Bi_2Se_3)_3$. We note, however, that the Ag–Ag distance in the periodic images in the y-direction is restricted to the length of the y-lattice vector, i.e., 4.26 Å; larger supercells are preferred to avoid artificial interactions between the dopant sites, which in the "real" material do not share the translational symmetry of the lattice.[36] However, a supercell that is $1 \times 2 \times 1$ times larger than the primitive cell will not only have larger number of total atoms but will also require simulating $_{44}C_4 = 135751$ configurations (four Ag atoms to be arranged in 44 cation sites). Since simulating all the configurations is beyond the capacity of present-day computational resources, we simulated nine representative configurations of a $1 \times 2 \times 1$ supercell. We find that the configurations where Ag atoms are distributed in both the layers have lower formation energies (see Supporting Information), consistent with experimental findings. However, the limitations on computing all relevant configurations preclude explanation of certain details, such as why Ag is uniformly distributed in Bi_2Se_3 layers but not in PbSe layers as shown in Figure 3a.

A structural analysis of all the 240 configurations (see Supporting Information) reveals that Ag dopants distort the lattice of the crystal and the configurations with lowest formation energies have minimal distortion in the crystal. A Bader charge analysis of the configurations shows that the low energy configurations have localized charge modulation around the Ag dopants. Large distortions in the lattice planes are expected when $(PbSe)_5(Bi_2Se_3)_3$ is doped with a high

concentration of Ag. This has been experimentally observed in the form of an instability when $(PbSe)_5(Bi_2Se_3)_3$ is doped with 25% Ag.[28] Most likely, these distortions are mediated by significantly lower charge of the Ag atoms in comparison to that of Bi and Pb cations (see Supporting Information for full discussion).

The observation of sharp peaks in the probability distribution of Figure 4b raises the question of whether there are correlations in the distribution of Ag atoms within and between layers. In other words, does the presence of a Ag atom influence the probability of finding another Ag atom nearby? To investigate correlations in the Ag distribution, the Ag–Ag radial distribution function (RDF) was generated from the APT data (Figure 4c). A RDF gives the probability of finding an atom B surrounding atom A as a function of distance.[37,38] The RDF was generated using data from the center of the reconstruction, which has been shown to improve the resolution[38] (Figure S5), and is plotted for distances greater than 0.2 nm because ion trajectory effects complicate interpretation at smaller distances.[37] The experimental Ag–Ag RDF shows an increased probability of finding Ag atoms ~7 Å apart, implying a pairwise correlation in Ag dopant distribution. In other words, the average distance from a given Ag atom to the next closest Ag atom is less than the average distance between Ag atoms. The significance of the variations in the experimental RDF can be evaluated by comparing with the fluctuations in RDFs of 10 simulated data sets of the same size but with *randomly* distributed Ag atoms ('+' markers, Figure 4c). Clearly, the spatial correlations observed in the APT data are not present in a random alloy. Figure S8 shows that the Ag–Ag pairing occurs primarily between Ag atoms in adjacent Bi_2Se_3 and PbSe sublayers by presenting RDF analyses within each sublayer (top and middle panels, Figure S8c: weakest correlations) and between sublayers (bottom panel, Figure S8c: strongest correlations).

To summarize, we have demonstrated that APT can provide new insights into the dopant distribution in 2D materials. APT has the potential to be applied to other 2D materials, such as transition metal dichalcogenides, and can therefore play an important role in the development of controlled doping schemes. First-principles DFT calculations can provide support for an understanding of experimental results and may be further employed to explain the origin of physical properties based on the dopant distribution confirmed by APT. The combination of APT and first-principles calculations has the potential to significantly advance knowledge of structure property relationships at the atomic and nanoscale.

■ **ASSOCIATED CONTENT**

ⓢ Supporting Information

The Supporting Information is available free of charge on the ACS Publications website at DOI: 10.1021/acs.nanolett.6b02104.

> Methods, calculation of interlayer bonding strength of $(PbSe)_5(Bi_2Se_3)_3$, influence of laser energy on $(PbSe)_5(Bi_2Se_3)_3$, APT analysis of $(PbSe)_5(Bi_2Se_3)_6$, structural and charge analysis of configurations contributing to 99.99% of total probabilities at 300 K, formation energies of representative $1 \times 2 \times 1$ supercell configurations, and analysis of Ag pairing (PDF)

AUTHOR INFORMATION

Corresponding Author
*E-mail: lauhon@northwestern.edu.

Notes
The authors declare no competing financial interest.

ACKNOWLEDGMENTS

ABBREVIATIONS

2D, two-dimensional; SEM, scanning electron microscopy; TEM, transmission electron microscopy; STEM, scanning transmission electron microscopy; SIMS, secondary ion mass spectrometry; APT, atom probe tomography; TMDs, transition metal dichalcogenides; DFT, density functional theory; FIB, focused ion beam; SDM, spatial distribution map; RDF, radial distribution function

REFERENCES

(1) Castro Neto, A. H.; Guinea, F.; Peres, N. M. R.; Novoselov, K. S.; Geim, A. K. The Electronic Properties of Graphene. *Rev. Mod. Phys.* **2009**, *81*, 109−162.

(2) Wang, Q. H.; Kalantar-Zadeh, K.; Kis, A.; Coleman, J. N.; Strano, M. S. Electronics and Optoelectronics of Two-Dimensional Transition Metal Dichalcogenides. *Nat. Nanotechnol.* **2012**, *7*, 699−712.

(3) Butler, S. Z.; Hollen, S. M.; Cao, L. Y.; Cui, Y.; Gupta, J. A.; Gutierrez, H. R.; Heinz, T. F.; Hong, S. S.; Huang, J. X.; Ismach, A. F.; et al. Progress, Challenges, and Opportunities in Two-Dimensional Materials Beyond Graphene. *ACS Nano* **2013**, *7*, 2898−2926.

(4) Xia, Y.; Qian, D.; Hsieh, D.; Wray, L.; Pal, A.; Lin, H.; Bansil, A.; Grauer, D.; Hor, Y. S.; Cava, R. J.; et al. Observation of a Large-Gap Topological-Insulator Class with a Single Dirac Cone on the Surface. *Nat. Phys.* **2009**, *5*, 398−402.

(5) Zhang, H. J.; Liu, C. X.; Qi, X. L.; Dai, X.; Fang, Z.; Zhang, S. C. Topological Insulators in Bi_2Se_3, Bi_2Te_3 and Sb_2Te_3 with a Single Dirac Cone on the Surface. *Nat. Phys.* **2009**, *5*, 438−442.

(6) Radisavljevic, B.; Radenovic, A.; Brivio, J.; Giacometti, V.; Kis, A. Single-Layer MoS_2 Transistors. *Nat. Nanotechnol.* **2011**, *6*, 147−150.

(7) Rycerz, A.; Tworzydlo, J.; Beenakker, C. W. J. Valley Filter and Valley Valve in Graphene. *Nat. Phys.* **2007**, *3*, 172−175.

(8) Schedin, F.; Geim, A. K.; Morozov, S. V.; Hill, E. W.; Blake, P.; Katsnelson, M. I.; Novoselov, K. S. Detection of Individual Gas Molecules Adsorbed on Graphene. *Nat. Mater.* **2007**, *6*, 652−655.

(9) Yin, Z. Y.; Li, H.; Li, H.; Jiang, L.; Shi, Y. M.; Sun, Y. H.; Lu, G.; Zhang, Q.; Chen, X. D.; Zhang, H. Single-Layer MoS_2 Photo-transistors. *ACS Nano* **2012**, *6*, 74−80.

(10) Withers, F.; Del Pozo-Zamudio, O.; Mishchenko, A.; Rooney, A. P.; Gholinia, A.; Watanabe, K.; Taniguchi, T.; Haigh, S. J.; Geim, A. K.; Tartakovskii, A. I.; et al. Light-emitting diodes by band-structure engineering in van der Waals heterostructures. *Nat. Mater.* **2015**, *14*, 301−306.

(11) Fang, H.; Tosun, M.; Seol, G.; Chang, T. C.; Takei, K.; Guo, J.; Javey, A. Degenerate n-Doping of Few-Layer Transition Metal Dichalcogenides by Potassium. *Nano Lett.* **2013**, *13*, 1991−1995.

(12) Suh, J.; Park, T.-E.; Lin, D.-Y.; Fu, D.; Park, J.; Jung, H. J.; Chen, Y.; Ko, C.; Jang, C.; Sun, Y.; et al. Doping against the Native Propensity of MoS2: Degenerate Hole Doping by Cation Substitution. *Nano Lett.* **2014**, *14*, 6976−6982.

(13) Gong, Y. J.; Liu, Z.; Lupini, A. R.; Shi, G.; Lin, J. H.; Najmaei, S.; Lin, Z.; Elias, A. L.; Berkdemir, A.; You, G.; et al. Band Gap Engineering and Layer-by-Layer Mapping of Selenium-Doped Molybdenum Disulfide. *Nano Lett.* **2014**, *14*, 442−449.

(14) Cheng, Y. C.; Zhu, Z. Y.; Mi, W. B.; Guo, Z. B.; Schwingenschlogl, U. Prediction of Two-Dimensional Diluted Magnetic Semiconductors: Doped Monolayer MoS_2 Systems. *Phys. Rev. B: Condens. Matter Mater. Phys.* **2013**, *87*, 100401.

(15) Zhang, K.; Feng, S.; Wang, J.; Azcatl, A.; Lu, N.; Addou, R.; Wang, N.; Zhou, C.; Lerach, J.; Bojan, V.; et al. Manganese Doping of Monolayer MoS_2: The Substrate Is Critical. *Nano Lett.* **2015**, *15*, 6586−6591.

(16) Laskar, M. R.; Nath, D. N.; Ma, L.; Lee, E. W.; Lee, C. H.; Kent, T.; Yang, Z.; Mishra, R.; Roldan, M. A.; Idrobo, J.-C.; et al. P-type Doping of MoS_2 Thin Films Using Nb. *Appl. Phys. Lett.* **2014**, *104*, 092104.

(17) Lin, Y.-C.; Dumcenco, D. O.; Komsa, H.-P.; Niimi, Y.; Krasheninnikov, A. V.; Huang, Y.-S.; Suenaga, K. Properties of Individual Dopant Atoms in Single-Layer MoS_2: Atomic Structure, Migration, and Enhanced Reactivity. *Adv. Mater.* **2014**, *26*, 2857−2861.

(18) Chou, H.; Ismach, A.; Ghosh, R.; Ruoff, R. S.; Dolocan, A. Revealing the planar chemistry of two-dimensional heterostructures at the atomic level. *Nat. Commun.* **2015**, *6*, 8229.

(19) Perea, D. E.; Hemesath, E. R.; Schwalbach, E. J.; Lensch-Falk, J. L.; Voorhees, P. W.; Lauhon, L. J. Direct Measurement of Dopant Distribution in an Individual Vapour-Liquid-Solid Nanowire. *Nat. Nanotechnol.* **2009**, *4*, 315−319.

(20) Moutanabbir, O.; Isheim, D.; Blumtritt, H.; Senz, S.; Pippel, E.; Seidman, D. N. Colossal Injection of Catalyst Atoms into Silicon Nanowires. *Nature* **2013**, *496*, 78−82.

(21) Cojocaru-Miredin, O.; Choi, P.; Wuerz, R.; Raabe, D. Atomic-Scale Characterization of the $CdS/CuInSe_2$ Interface in Thin-Film Solar Cells. *Appl. Phys. Lett.* **2011**, *98*, 103504.

(22) Kambham, A. K.; Mody, J.; Gilbert, M.; Koelling, S.; Vandervorst, W. Atom-Probe for FinFET Dopant Characterization. *Ultramicroscopy* **2011**, *111*, 535−539.

(23) Kambham, A. K.; Kumar, A.; Florakis, A.; Vandervorst, W. Three-Dimensional Doping and Diffusion in Nano Scaled Devices as Studied by Atom Probe Tomography. *Nanotechnology* **2013**, *24*, 275705.

(24) Hor, Y. S.; Williams, A. J.; Checkelsky, J. G.; Roushan, P.; Seo, J.; Xu, Q.; Zandbergen, H. W.; Yazdani, A.; Ong, N. P.; Cava, R. J. Superconductivity in $Cu_xBi_2Se_3$ and its Implications for Pairing in the Undoped Topological Insulator. *Phys. Rev. Lett.* **2010**, *104*, 057001.

(25) Kanatzidis, M. G. Structural Evolution and Phase Homologies for "Design" and Prediction of Solid-State Compounds. *Acc. Chem. Res.* **2005**, *38*, 359−368.

(26) Nakayama, K.; Eto, K.; Tanaka, Y.; Sato, T.; Souma, S.; Takahashi, T.; Segawa, K.; Ando, Y. Manipulation of Topological States and the Bulk Band Gap Using Natural Heterostructures of a Topological Insulator. *Phys. Rev. Lett.* **2012**, *109*, 236804.

(27) Sasaki, S.; Segawa, K.; Ando, Y. Superconductor Derived from a Topological Insulator Heterostructure. *Phys. Rev. B: Condens. Matter Mater. Phys.* **2014**, *90*, 220504.

(28) Nakayama, K.; Kimizuka, H.; Tanaka, Y.; Sato, T.; Souma, S.; Takahashi, T.; Sasaki, S.; Segawa, K.; Ando, Y. Observation of Two-Dimensional Bulk Electronic States in the Superconducting Topological Insulator Heterostructure $Cu_x(PbSe)_5(Bi2Se3)_6$: Implications for Unconventional Superconductivity. *Phys. Rev. B: Condens. Matter Mater. Phys.* **2015**, *92*, 100508.

(29) Fang, L.; Stoumpos, C. C.; Jia, Y.; Glatz, A.; Chung, D. Y.; Claus, H.; Welp, U.; Kwok, W. K.; Kanatzidis, M. G. Dirac Fermions and Superconductivity in the Homologous Structures $(Ag_xPb_{1-x}Se)_5(Bi2Se3)_{3m}$ (m = 1,2). *Phys. Rev. B: Condens. Matter Mater. Phys.* **2014**, *90*, 020504.

(30) Fu, L.; Kane, C. L. Superconducting Proximity Dffect and Majorana Fermions at the Surface of a Topological Insulator. *Phys. Rev. Lett.* **2008**, *100*, 096407.

(31) Thompson, K.; Lawrence, D.; Larson, D. J.; Olson, J. D.; Kelly, T. F.; Gorman, B. In situ Site-Specific Specimen Preparation for Atom Probe Tomography. *Ultramicroscopy* **2007**, *107*, 131−139.

(32) Gruber, M.; Vurpillot, F.; Bostel, A.; Deconihout, B. Field Evaporation: A Kinetic Monte Carlo Approach on the Influence of Temperature. *Surf. Sci.* **2011**, *605*, 2025−2031.

(33) Gault, B.; Moody, M. P.; Cairney, J. M.; Ringer, S. P. Atom Probe Crystallography. *Mater. Today* **2012**, *15*, 378−386.

(34) Baik, S.-I.; Ma, L.; Kim, Y.-J.; Li, B.; Liu, M.; Isheim, D.; Yakobson, B. I.; Ajayan, P. M.; Seidman, D. N. An Atomistic Tomographic Study of Oxygen and Hydrogen Atoms and their Molecules in CVD Grown Graphene. *Small* **2015**, *11*, 5968−5974.

(35) Shelimova, L. E.; Karpinskii, O. G.; Zemskov, V. S. X-Ray Diffraction Study of Ternary Layered Compounds in the $PbSe-Bi_2Se_3$ System. *Inorg. Mater.* **2008**, *44*, 927−931.

(36) Freysoldt, C.; Grabowski, B.; Hickel, T.; Neugebauer, J.; Kresse, G.; Janotti, A.; Van de Walle, C. G. First-principles calculations for point defects in solids. *Rev. Mod. Phys.* **2014**, *86*, 253.

(37) Sudbrack, C. K.; Noebe, R. D.; Seidman, D. N. Direct Observations of Nucleation in a Nondilute Multicomponent Alloy. *Phys. Rev. B: Condens. Matter Mater. Phys.* **2006**, *73*, 212101.

(38) Haley, D.; Petersen, T.; Barton, G.; Ringer, S. P. Influence of Field Evaporation on Radial Distribution Functions in Atom Probe Tomography. *Philos. Mag.* **2009**, *89*, 925−943.

Supporting Information

Atom Probe Tomography Analysis of Ag Doping in 2D Layered Material $(PbSe)_5(Bi_2Se_3)_3$

Xiaochen Ren[†], Arunima K. Singh[||], Lei Fang[||,^], Mercouri G. Kanatzidis[||,^], Francesca Tavazza[||],

Albert V. Davydov[||], and Lincoln J. Lauhon*,[†]

[†]Department of Materials Science and Engineering, Northwestern University, 2220 Campus

Drive, Evanston, Illinois 60208, United States

[||]Materials Science and Engineering Division, National Institute of Standards and Technology,

100 Bureau Drive, Gaithersburg, Maryland 20899, United States

[||]Department of Chemistry, Northwestern University, 2145 Sheridan Road, Evanston, Illinois

60208, United States

^ Materials Science Division, Argonne National Laboratory, 9700 South Cass Avenue, Argonne,

Illinois 60439, United States

*E-mail: lauhon@northwestern.edu.

List of Contents

1. Additional Details on Methods

Precursors PbSe and Bi_2Se_3 were made by solid-state synthesis using high-purity elements (American Elements, purity>99.999%). Then, Ag, PbSe and Bi_2Se_3 were weighted in a nominal composition $Ag_xPb_5Bi_6Se_{14}$ (x~1) and ground thoroughly. The mixture was sealed in an evacuated quartz tube and loaded in a tube furnace. The furnace was first heated to 950 °C over 12 h and then held at this temperature for 12 h. Subsequently, the furnace was cooled to 650 °C over 80 h and then shut off.

Specimens for atom probe tomography (APT) analysis were prepared using standard focused ion beam (FIB) lift-out and sharpening procedures using e-beam deposited Pt as a capping layer, with the analysis direction perpendicular to (001) planes. APT was performed using a LEAP 4000X Si with a 355 nm laser at 250 kHz pulse frequency, a 0.005 ions/pulse target detection rate, a background temperature of 28 K, and laser pulse energies between 1 and 30 pJ. There were several IEC events at the beginning of analyses, presumably related to the interface between capping layer and the material. Once started, the evaporation ran steadily. The multiple hit ratio is relatively high for this material, varying non-monotonically between 66% and 71% at 30 pJ and between 62% and 68% at 10 pJ. The multiple hit ratio decreases slightly when laser power is lower, but it doesn't change significantly. Reconstructions and analyses were conducted using the commercial software package IVAS. Reconstruction was done using tip-profile method with detection efficiency of 0.5 and k-factor of 3.3. The image compression factor (ICF) was adjusted to tune the lattice spacing in analysis direction. The lattice spacing matched the expected value of 1.65 nm when the ICF is between 1.9 and 2.1, depending on the run. The

reported analysis was based on a reconstruction with ICF = 2.1. Radial distribution functions of simulated data were calculated by importing the simulation results into IVAS.

All simulations are based on density functional theory (DFT) using the projector augmented wave method as implemented in the plane-wave code VASP*[1].[1-4] For the structural relaxations and energy calculations, we employed the optB88-vdW-DF functional, which includes van der Waals (vdW) interactions.[5-8] Relaxations of the structures were performed until the forces and in-plane stresses were below 5 meV/Å and 0.01 GPa, respectively. The Brillouin zone integration was performed using k-point meshes with > 32 points $Å^{-1}$ and a Gaussian smearing with a width of 0.05 eV. Such a k-point mesh and a cutoff energy of 550 eV ensure convergence of the total energies to better than 1 meV per unit cell. $(PbSe)_5(Bi_2Se_3)_3$ adopts a layered structure with monoclinic space group P21/m, where PbSe and Bi_2Se_3 layers are separated by weak van der Waals forces. The lattice parameters obtained from DFT structural relaxations, a = 16.3312 Å, b = 4.2635 Å, c = 21.9245 Å, $\alpha = \gamma$ = 90 ° and β = 96.668 °, are within 2.5 % of the experimentally measured values. [9]

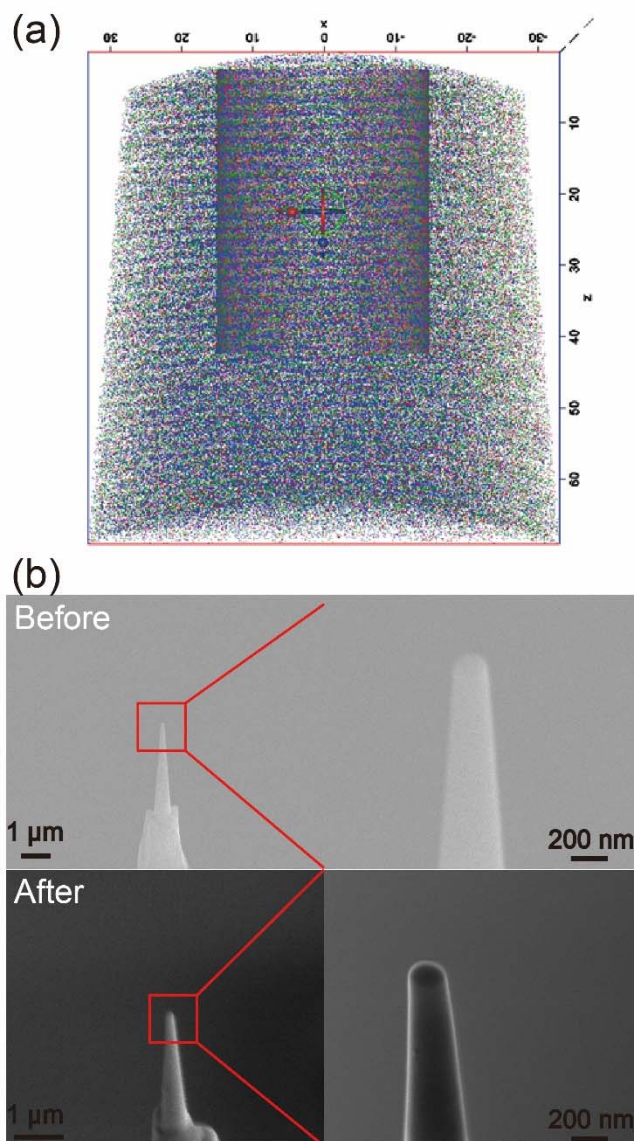* Reference to specific software packages does not imply a NIST endorsement.

Figure S1 (a) Image of the overall resconstruction with Bi (blue), Pb(green) and Ag (red) atoms shown. The cylinder defines the region of interest (ROI), from which Figure 1d was generated. (b) A comparison of tip shapes before and after LEAP analysis with a 20 pJ pulse energy, showing that the tip shape does not change significantly.
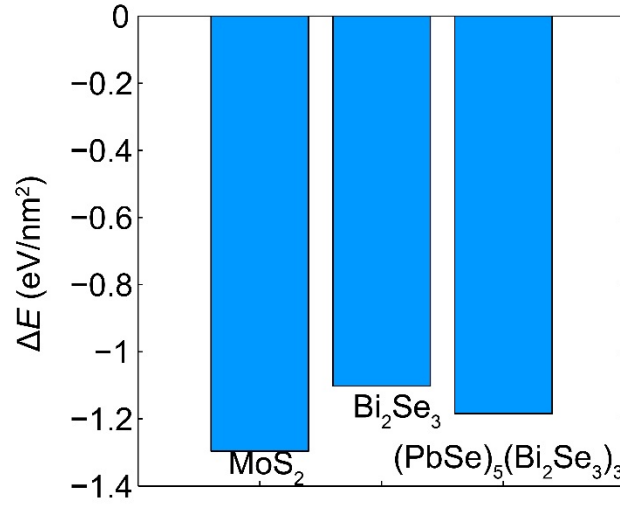
2. Interlayer Interaction Strength of $(PbSe)_5(Bi_2Se_3)_3$

Figure S2 Interlayer interactions strength in layered MoS_2, Bi_2Se_3 and $(PbSe)_5(Bi_2Se_3)_3$.

The interlayer interaction energies, ΔE, in layered materials can be computed as, $\Delta E = \dfrac{\frac{Energy\ of\ bulk\ material}{\#\ surfaces} - \frac{Energy\ of\ individual\ layers}{\#\ surfaces}}{Surface\ Area}$. The structural relaxations of the individual surfaces are performed

with a vacuum spacing larger than 18 Å. In Figure S2, we compare the interlayer interaction

energies of $(PbSe)_5(Bi_2Se_3)_3$ to those of bulk MoS_2 and bulk Bi_2Se_3, both of which are van der

Waals bonded layered materials.[10] Clearly, the interactions between adjacent layers in

$(PbSe)_5(Bi_2Se_3)_3$ are comparable to that of MoS_2 and Bi_2Se_3, thus, are in the range of van der

Waals interactions.

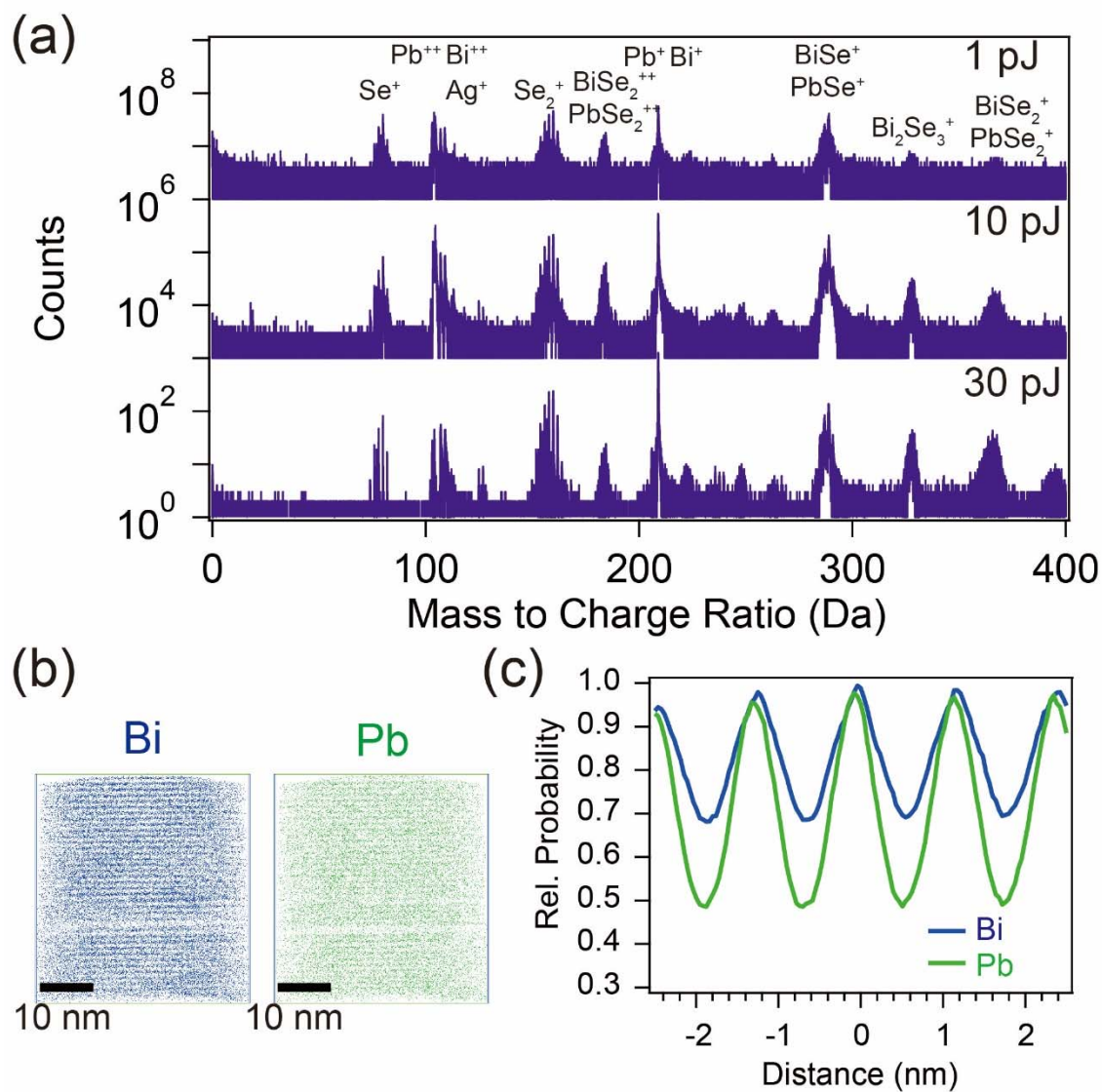## 3. Influence Of Laser Pulse Energy On Spatial Resolution

Figure S3 (a) Mass spectra acquired under different laser energies (curves are offset for clarity). (b) Images of reconstruction from data taken at 10 pJ laser pulse energy. (c) SDM of Bi and Pb relative to Bi atoms from reconstruction shown in (b).

The laser pulse energy does not have a dramatic influence on the mass spectrum within the range of pulse energies considered (SI Fig. 3a). However, alternating PbSe and Bi_2Se_3 layers were not resolved at 1 pJ or 10 pJ. The reconstruction and SDM taken at 10 pJ are shown in Figure S3b and S3c. The poor resolution is likely associated with the preferential field induced loss of Pb. At 30 pJ, layers were resolved as described in the main text.
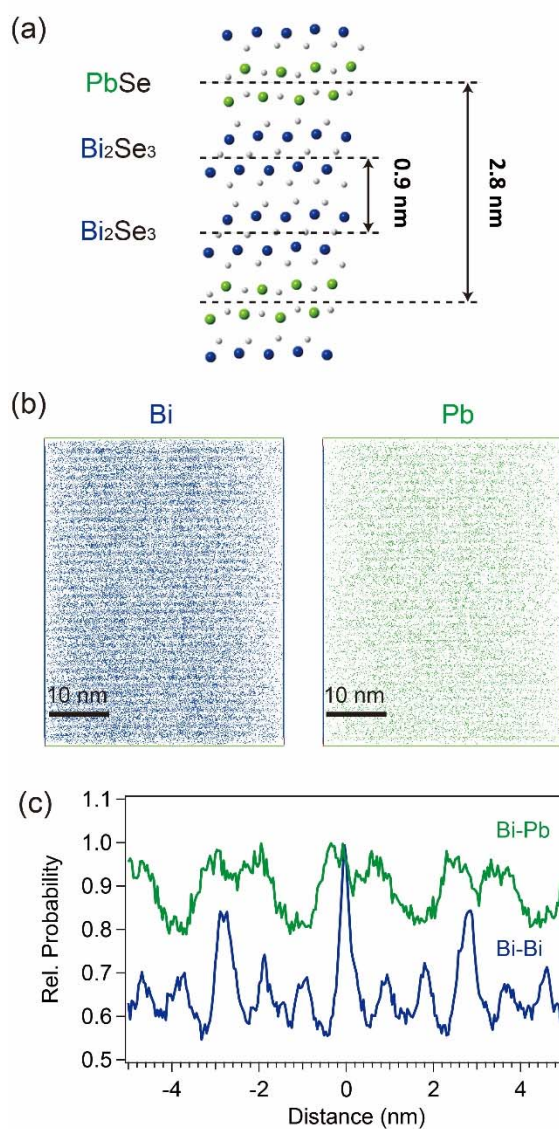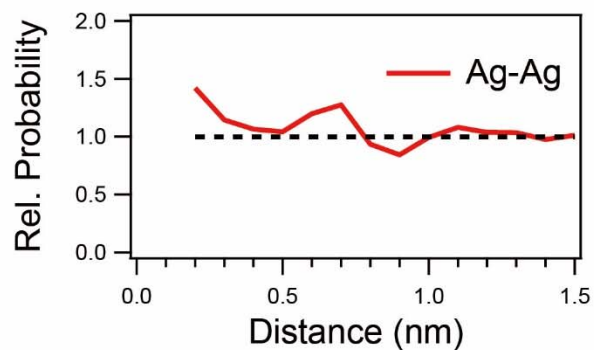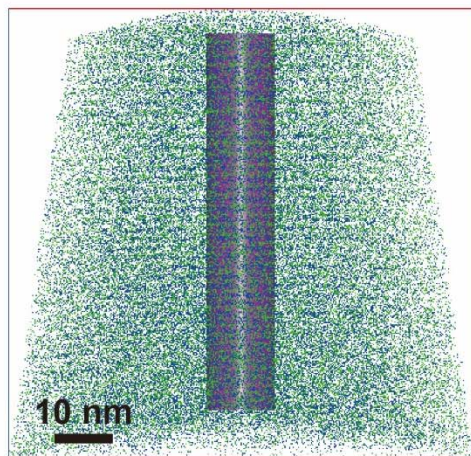
4. APT analysis of Ag doped $(PbSe)_5(Bi_2Se_3)_6$

Figure S4 (a) Crystal structure of $(PbSe)_5(Bi_2Se_3)_6$. (b) Reconstruction of Ag doped $(PbSe)_5(Bi_2Se_3)_6$. (c) SDM of Bi and Pb relative to Bi atoms.

Ag doped $(PbSe)_5(Bi_2Se_3)_6$ was also analyzed by APT. SDM analysis resolves PbSe layers alternating with two layers of Bi_2Se_3.

5. Radial Distribution Function (RDF) in different regions of interest (ROIs)
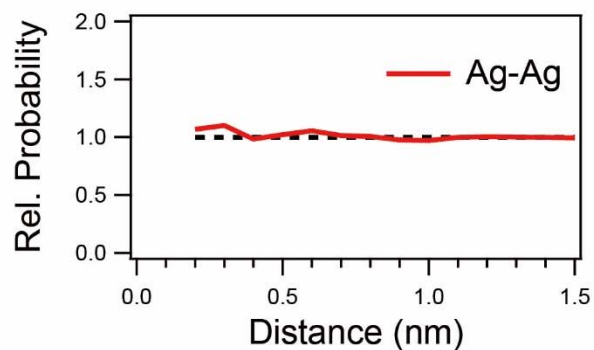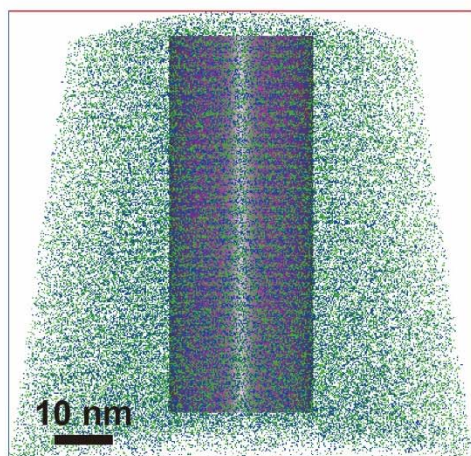

Figure S5 (a) RDF within a cylindrical ROI of 12 nm diameter. (b) RDF within a cylindrical ROI of 30 nm diameter.

RDF quality is higher when the ROI is confined in the pole region, extracting short-range order information. This finding is in agreement with the work of Ringer *et al.*[11].

6. Structural and Charge Analysis of Configurations Contributing to 99.99 % of the Total Probabilities at 300 K

In order to understand why some configurations are more stable than the others we analyzed the structures, specifically the local coordination around Ag atoms, and the charge distribution for all the 231 configurations. We computed the charges on the individual atoms using the Bader formalism[12]. Figure S6 (a)-(h) show a ball and stick model of the configurations and Figure S6 (i)-(viii) show the magnitude of charges on the atoms.

Among all the 231 configurations, the configurations shown in Figure S6 (a)-(g) (or (i)-(vii)) account for more than 99.99 % of the total probabilities at room temperature. The configuration shown in Figure S6 (h) (or (viii)) corresponds to a high energy configuration, with configuration formation energies at least 0.5 eV larger than that of configurations (a)-(g). Notably, along the z direction, the Ag atoms distort the Bi- and Pb-chains much less in (a)-(g) than in the high-energy configuration (h). An analysis of all the configurations shows that the correlation between the formation energies and distortion of the existing Pb- or Bi-chains is very weak. While most of the lower energy configurations do have less distortion in the Pb- and Bi-chains, we find that some high-energy configurations have similarly low distortion in the structure.
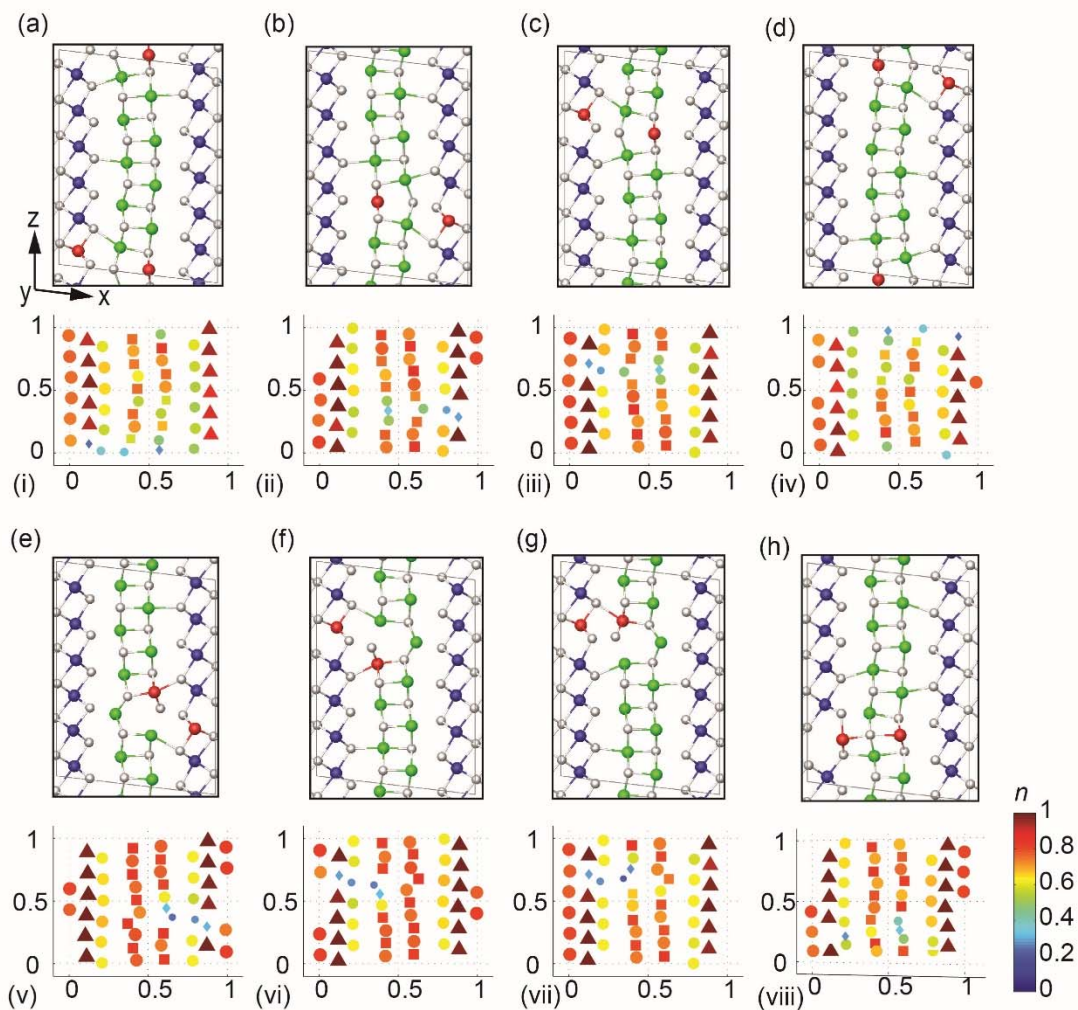
Figure S6 (a)-(h) Ball and stick model of Ag doped $(PbSe)_5(Bi_2Se_3)_3$ configurations. Ag, Se, Pb and Bi atoms are represented by red, white, green and blue spheres, respectively. The primitive cell region is marked with gray lines. (i)-(viii) The magnitude of charges, n, on all atoms of the configuration shown directly above each plot. The charge distribution is projected onto the x-z plane of the primitive cell and scaled coordinates are used for atomic locations. Symbol sizes and colors denote the magnitude of charges on each atom. Ag, Se, Pb and Bi atoms are represented by diamond, circle, square and traingle symbols, respectively.

A weak correlation in the charge modulation around the Ag atoms and formation energy is observed. Configurations where the charge modulation is localized around the Ag atoms, such as Figure S6 (vi), generally have lower formation energies, however, many exceptions were found, for *e.g.* in Figure S6 (viii). The charges on Bi atoms in undoped $(PbSe)_5(Bi_2Se_3)_3$ are positive and vary between 0.96 to 0.99. The Pb atoms are positively charged as well with a smaller charge variation between 0.80 to 0.81. However, in the Ag substituted configurations, the Ag atoms while positively charged, have a much smaller charge ranging between 0.07 to 0.51. The considerably difference in the charges of the Ag atoms in comparison to that of the Pb and Bi cations is the likely cause of distortion og the lattice upon Ag substitution. This is in agreement with the experimental observations where more than 25 % substitution of Ag in $(PbSe)_5(Bi_2Se_3)_3$ renders the materials unstable[9].

7. Simulations with Larger Cell Sizes

To circumvent the problem of a short distance of 4.26 Å in the periodic images of Ag atoms in the *y* direction for the simulations performed on the primitive cell configurations, we assessed the possibility of using larger simulation cells. Using a supercell with 1X2X1 times larger than the primitive cell results in 44 cation substitutional sites and 4 Ag atoms to be substituted in those sites to simulate a ~20 % Ag substitution. The resultant number of configurations, $^{44}C_4 = 135751$, is very large and beyond the practical simulation capacity of present-day computational resources. We analyzed the charge density and charges on the atoms of undoped $(PbSe)_5(Bi_2Se_3)_3$ to identify any similar cation sites to reduce the number of substitutional sites. However, the charge density and charge distribution around the cations are complex. The

difference in lattice and symmetry of the individual PbSe (orthorhombic[13]) and Bi_2Se_3 (hexagonal[14]) layers most likely creates the large monoclinic primitive cell for the layered $(PbSe)_5(Bi_2Se_3)_3$ with large undulations in the individual layers.

Since reduction in the number of substitutional sites or simulating all the configurations is infeasible, we simulated 9 representative configurations of the 1X2X1 cell. Figure S7 (i)-(v) shows the configurations where Ag atoms were distributed in both the PbSe and Bi_2Se_3 layers. While (i) is a configuration where all the Ag atoms are localized, (ii)-(iii) have Ag atoms located far apart and equally distributed in both the layers. In configuration (iv), there are more Ag atoms in the Bi_2Se_3 layer and vice versa in (v). Ag atoms are restricted to the PbSe layer in (vi) and (vii), and the Ag atoms are localized in the former but are well-spaced in the later. Similarly, (viii) has localized Ag atoms in the Bi_2Se_3 layer and the Ag atoms are well spaced in (ix).

Figure S7 shows the formation energies, ΔE_{Ag}^i, of the configurations with 1X2X1 cell normalized to the units of eV/primitive cell. The formation energies of the configurations with 1X2X1 cell are comparable to the formation energies found for the configurations with the 1X1X1 cell.

The lowest energy configuration is found to be (v) and its formation energy is smaller than the formation energies sampled in the 1X1X1 cell. A conclusive statement cannot be made about the preferability of Ag atoms based on this small sample space. Nonetheless, the simulations performed for 1X1X1 cells and the results for this small sample size show a bias for Ag atoms to be preferably distributed between the PbSe and Bi_2Se_3 layers. With the enormous progress in

computing platforms and computational methods, the challenge of simulating more structures for a comprehensive evaluation could be tackled in the near future.
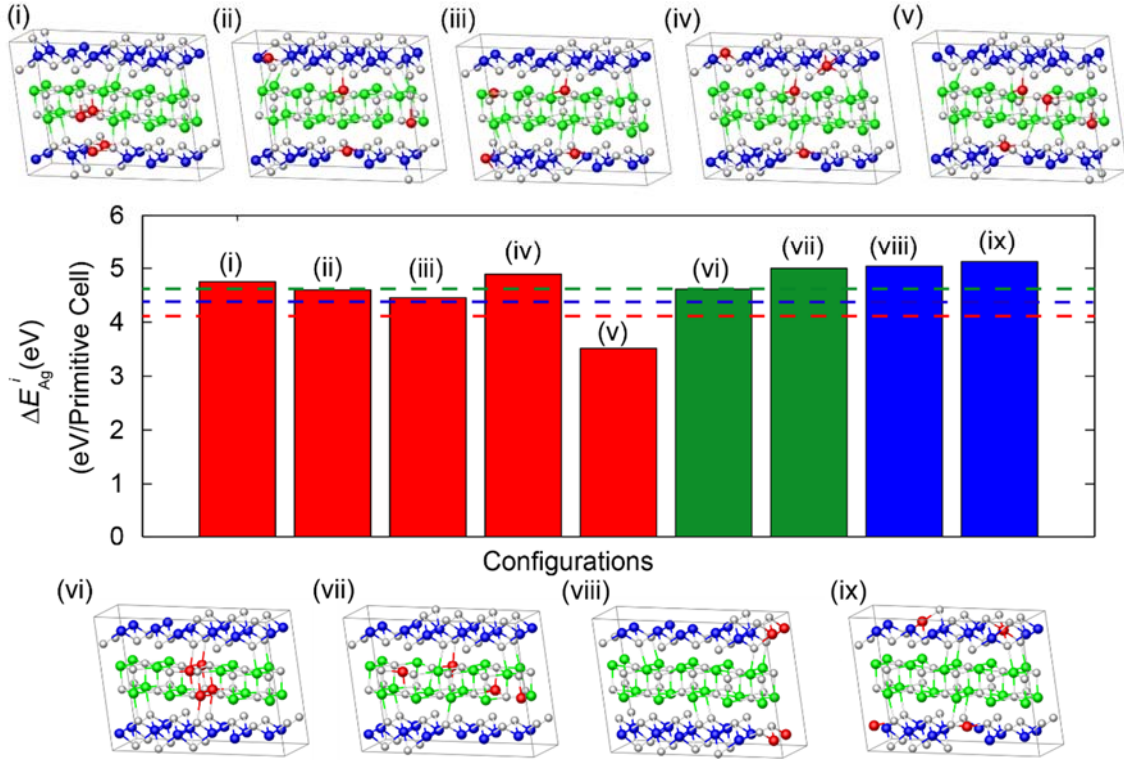

Figure S7 (i)-(ix) show the 9 representative configurations of Ag doped $(PbSe)_5(Bi_2Se_3)_3$ for a 1X2X1 cell. Ag, Se, Pb and Bi atoms are represented by red, white, green and blue spheres, respectively. The 1X2X1 cell is shown as a gray box. The bar plot shows the formation energies in these configurations. Red, green and blue bars denote the formation energies of configurations with Ag atoms distribtuted between PbSe and Bi_2Se_3 layers, Ag atoms restricted to PbSe layer and Ag atoms restricted to Bi_2Se_3 layer, respectively. The lowest formation energies computed from the configurations of the 1X1X1 cell are shown as dotted lines. The dotted red, green and blue lines represent the formation energy of the lowest energy configuration for Ag distributed between PbSe and Bi_2Se_3 layers, Ag atoms restricted to PbSe layer and Ag atoms restricted to Bi_2Se_3 layer, respectively.
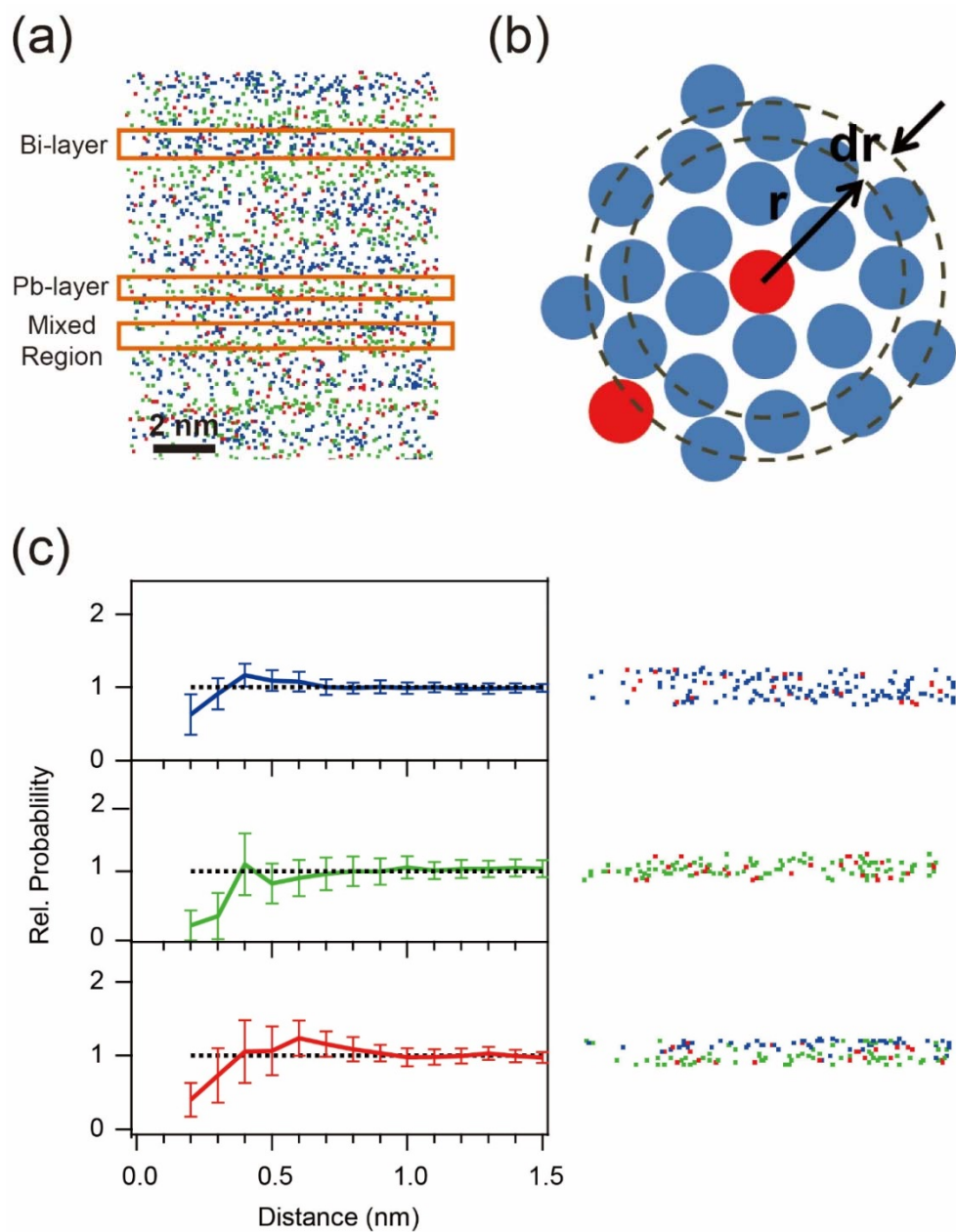
8. 2D RDF Analysis of Ag pairing

Figure S8 (a) ROI and selection of Bi-layer, Pb-layer and mixed region. (b) Schematic of 2D RDF. (c) 2D RDF from Bi-layers (blue), Pb-layers (green) and mixed regions (red).

2D RDF analysis was conducted in Matlab with a custom code. For the distribution of atoms of species i around given species j, the RDF was calculated as:

$$RDF_{i,j}(\mathrm{r}) = \frac{1}{C_0} \sum_{k=1}^{N_j} \frac{N_k^i(r)}{N_k^{tot}(r)}.$$

Where C_0 is the overall concentration of species i in the analyzed volume, N_j is the number of atoms of species j in the analyzed volume, $N_k^i(r)$ is the number of atoms of species i in a radius of r around the kth atom of species j, and $N_k^{tot}(r)$ is the total number of atoms in a radius of r around the kth atom of species j. For 2D RDF, Z coordinates are ignored. Thus $\mathrm{r} = \sqrt{x^2 + y^2}$.

2D RDFs were calculated to examine correlations between Ag atoms within and between layers. Ag-Ag 2D RDFs were generated from 10 Bi-layers, 10 Pb-layers and 10 mixed regions. The averages of the distributions are shown in Figure S8 (c). The error bars show the uncertainty arising from counting statistics, i.e. the finite number of counts within a particular distance bin. The strongest positive correlation is between Ag atoms in Pb and Bi layers (red).

REFERENCES:

1. Kresse, G; Hafner, J. Ab initio Molecular Dynamics for Liquid Metals. *Phys. Rev. B*, **1993**, 47, 588.

2. Kresse, G; Hafner, J. Ab initio Molecular-Dynamics Simulation of the Liquid-Metal-Amorphous-Semiconductor Transition in Germanium. *Phys. Rev. B*, **1994**, 49, 14251.

3. Kresse, G.; Furthmüller, J. Efficiency of ab-initio Total Energy Calculations for Metals and Semiconductors Using a Plane-Wave Basis Set. *Comput. Mat. Sci.*, **1996**, 6, 15.

4. Kresse, G.; Furthmüller, J. Efficient Iterative Schemes for ab initio Total-Energy Calculations using a Plane-Wave Basis Set. *Phys. Rev. B*, **1996**, 54,11169.

5. Dion, M; Rydberg, H; Schröder, E; Langreth, D. C.; Lundqvist, B. I. van der Waals Density Functional for General Geometries. *Phys. Rev. Lett.* **2004**, 92, 246401.

6. Román-Pérez, G.; Soler, J. M. Efficient Implementation of a van der Waals Density Functional: Application to Double-Wall Carbon Nanotubes. *Phys. Rev. Lett.* **2009**, 103, 096102.

7. Klimeš, J.; Bowler, D. R.; Michaelides, A. Chemical Accuracy for the van der Waals Density Functional. *J. Phys.: Cond. Matt*. **2010**, 22, 022201.

8. Klimeš, J.; Bowler, D. R.; Michaelides, A. Van der Waals Density Functionals Applied to Solids. *Phys. Rev. B* **2011**, 83, 195131.

9. Fang, L.; Stoumpos, C. C.; Jia, Y.; Glatz, A.; Chung, D. Y.; Claus, H.; Kanatzidis, M. G. Dirac fermions and superconductivity in the homologous structures $(Ag_xPb_{1-x}Se)_5(Bi_2Se_3)_{3m}$(m= 1, 2).*Phys. Rev. B* **2014**, *90*, 020504.

10. Geim, A. K.; Grigorieva, I. V. Van der Waals Heterostructures. *Nature* **2013** 499, 419-425.

11. Haley, D.; Petersen, T.; Barton, G.; Ringer, S. P. Influence of Field Evaporation on Radial Distribution Functions in Atom Probe Tomography. *Philos. Mag.* **2009**, 89, 925-943.

12. Tang, W., E.; Henkelman, S. G. A Grid-based Bader Analysis Algorithm Without Lattice Bias. *J. Phys.: Cond. Matt*. **2009**, 21, 084204.

13. Singh, A. K.; Hennig, R. G. Computational Prediction of Two-Dimensional Group-IV Mono-Chalcogenides. *Appl. Phys. Lett.* **2014**, 105, 042103.

14. Zhang, Haijun, Chao-Xing Liu, Xiao-Liang Qi, Xi Dai, Zhong Fang, and Shou-Cheng Zhang. Topological Insulators in Bi_2Se_3, Bi_2Te_3 and Sb_2Te_3 with a Single Dirac Cone on the Surface. *Nat. Phys.* **2009**, 5, 438-442.